Lithospheric Erosion in the Patagonian Slab Window, and Implications for Glacial Isostasy

Hannah F. Mark[1,*†], Douglas A. Wiens[1], Erik R. Ivins[2], Andreas Richter[3], Walid Ben Mansour[1], M. Beatrice Magnani[4], Eric Marderwald[3], Rodrigo Adaros[5], Sergio Barrientos[6]

[1]Department of Earth and Planetary Sciences, Washington University in St. Louis; [2]Jet Propulsion Laboratory, California Institute of Technology; [3]Laboratorio MAGGIA, Universidad Nacional de La Plata; CONICET; [4]Southern Methodist University; [5]Empresa Nacional del Petróleo, Magallanes; [6]Centro Sismológico Nacional, Universidad de Chile

*Corresponding author: Hannah Mark, hmark@seismo.wustl.edu

†Now at the Woods Hole Oceanographic Institution

Key Points:

- We observe anomalously low upper mantle shear wave velocities (less than 4.1 km/s) in the Patagonian slab window
- The lithospheric mantle has been thermally eroded over the youngest part of the slab window
- Low viscosities in the slab window link observed rapid geodetic uplift to geologically recent ice mass loss in Patagonia

Abstract

The Patagonian slab window has been proposed to enhance the solid Earth response to ice mass load changes in the overlying Northern and Southern Patagonian Icefields (NPI and SPI, respectively). Here we present the first regional seismic velocity model covering the entire north-south extent of the slab window. A slow velocity anomaly in the uppermost mantle indicates warm mantle temperature, low viscosity, and possibly partial melt. Low velocities just below the Moho suggest that the lithospheric mantle has been thermally eroded over the youngest part of the slab window. The slowest part of the anomaly is north of 49°S, implying that the NPI and the northern SPI overlie lower viscosity mantle than the southern SPI. This comprehensive seismic mapping of the slab window provides key evidence supporting the previously hypothesized connection between post-Little Ice Age anthropogenic ice mass loss and rapid geodetically observed glacial isostatic uplift (≥ 4 cm/yr).

Plain Language Summary

A gap in the subducting plate beneath Patagonia has enabled hotter, less viscous mantle material to flow underneath South America. Icefields in the Austral Andes above the gap in the plate have recently been shrinking, removing weight that had caused the continent to flex downward. We use seismic data to image the subsurface structure and find very low seismic velocity within and around the gap, as well as thinning of the rigid South American lithosphere overlying the gap. The low mantle velocity implies that mantle viscosity is also low beneath the shrinking icefields, and low viscosity enables the region to rebound upwards.

1 Introduction

Slab windows form when a spreading ridge subducts and the plates continue to diverge, opening a gap in the subducting plate interface (Groome & Thorkelson, 2009; Thorkelson, 1996). Volcanic products associated with several Cenozoic slab windows can be found at subduction margins around the Pacific Ocean, indicating that this phenomenon is widespread (McCrory et al., 2009). The Patagonian slab window began forming ~18 Ma, when the Chile Ridge started subducting beneath South America near 54°S (Breitsprecher & Thorkelson, 2009). The Chile Triple Junction (CTJ) has since migrated north to its present-day location offshore the Península de Taitao near 46.5°S. Expressions of the slab window include gaps in arc volcanism and subduction zone seismicity (Agurto-Detzel et al., 2014; DeLong et al., 1979); adakitic volcanism near slab edges (Bourgois et al., 2016; Gorring et al., 1997; Stern & Kilian, 1996; Thorkelson & Breitsprecher, 2005); near-trench volcanic activity (Forsythe et al., 1986; Guivel et al., 2003; Marshak & Karig, 1977); anomalously high heat flow (Ávila & Dávila, 2018; Cande et al., 1987) and low upper mantle seismic velocity (Gallego et al., 2010; Russo, VanDecar, et al., 2010); positive dynamic topography (Georgieva et al., 2016; Guillaume et al., 2009) associated with low-viscosity asthenospheric mantle upwelling (Boutonnet et al., 2010; Gorring et al., 1997); and mantle flow patterns influenced by the slab window geometry (Murdie & Russo, 1999; Russo, Gallego, et al., 2010; Russo, VanDecar, et al., 2010). Volcanic products associated with several Cenozoic slab windows can be found at subduction margins around the Pacific Ocean, indicating that this phenomenon is widespread (McCrory et al., 2009).

The extent of the Patagonian slab window has previously been estimated based on plate kinematic reconstructions (Breitsprecher & Thorkelson, 2009) and has been mapped using body wave tomography in the immediate vicinity of the CTJ (Russo, VanDecar, et al., 2010). These

two methods are in good agreement near the CTJ (Figure 1), but the full extent of the slab window remains poorly defined. Reconciling tectonic reconstructions with observations such as the locations of slab-edge adakitic volcanism requires invoking ridge jumps and changes in spreading rates, which are poorly constrained due to the subduction of seafloor magnetic anomaly records (Bourgois et al., 2016).

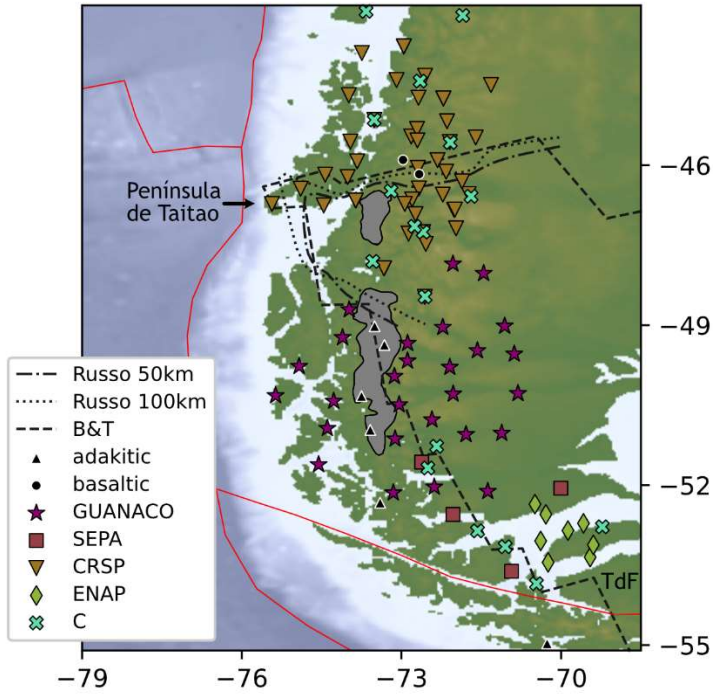

Figure 1: Map of the study region in Patagonia. Seismic stations and volcanoes are marked. Data sources are described in Section 2. Previously estimated slab window extents are shown for Russo, VanDecar, et al. (2010) and for Breitsprecher and Thorkelson (2009). The present-day NPI and SPI are shaded in grey (Davies et al., 2020) . Background map colors show bathymetry and elevation data (Ryan et al., 2009). Red lines show present-day plate boundaries. Tierra del Fuego (TdF) and the Península de Taitao are labeled.

The co-location of the Patagonian slab window with the Northern and Southern Patagonian Icefields (NPI and SPI) in the Austral Andes makes Patagonia an excellent place to study the effects of lateral variations in Earth structure on glacial isostatic adjustment (GIA). Low-viscosity mantle in the slab window beneath the icefields is expected to speed the GIA response to ice mass changes on decadal to centennial timescales, and ongoing glacial unloading is thought to drive extremely high uplift rates (up to 40 mm/yr) measured in the NPI and SPI (Dietrich et al., 2010; Ivins & James, 2004; Klemann et al., 2007; Lange et al., 2014; Richter et al., 2016). Improved constraints on the extent of the slab window and on lateral variations in the viscosity structure of the mantle beneath the icefields are necessary for improving GIA models and interpreting geodetic observations in terms of changing ice mass. More robust GIA models provide stronger constraints on past icefield mass and climate change (Oerlemans, 2005).

While surface volcanism provides some information on slab window formation and geometry, reliably reconstructing slab window mantle dynamics is a long-standing challenge in geodynamics (Dickinson, 1981; S. Lin, 2014). Seismic tomography is an essential tool for

connecting surface features to subsurface structure. In this study, we use seismic data recently collected by the GUANACO broadband seismic deployment to derive a new seismic velocity model for Patagonia, map the full extent of the slab window, and investigate how associated mantle dynamics have affected the overriding lithosphere. We show that the dynamics of the slab window are responsible for inferred low viscosities in the upper mantle and the unusually rapid glacial isostatic response to ice mass loss in the region.

2 Data and methods

We obtained a shear velocity (V_{sv}) model for Patagonia by jointly inverting Rayleigh wave dispersion curves from ambient noise and earthquake tomography with P receiver functions in a Bayesian framework that enables us to quantify velocity uncertainties statistically. Data were from the GUANACO (Magnani et al., 2020), SEPA (Wiens et al., 1998), and CRSP (Russo, VanDecar, et al., 2010) temporary seismic networks; and from the Chilean National Seismic Network, the GEOSCOPE Network, the Antarctic Seismographic Argentinian Italian Network, and ENAP (Empresa Nacional del Petróleo) monitoring stations.

2.1 Rayleigh wave tomography from ambient noise and earthquake records

We used ambient noise tomography to obtain isotropic Rayleigh wave phase velocities at 8 to 40 seconds period, and group velocities from 10 to 30 seconds (Bensen et al., 2007) (Figure S1). Temporal normalization was done with the running average method, and we incorporated time-frequency phase weighted stacking of the daily cross-correlation records (Schimmel et al., 2011; Schimmel & Gallart, 2007). We then obtained dispersion curves from the stacked cross-correlations using Automated Frequency Time Analysis (Bensen et al., 2007) and performed tomography using the method of Barmin et al. (2001). Uncertainties were estimated using a scaling relationship with ray path coverage, with group velocity uncertainties taken to be double the phase velocity uncertainties (Barmin et al., 2001; Shen et al., 2016).

Surface wave tomography was performed using shallow events (<50 km depth) within 20-150° of the study region (Figure S2). A balanced azimuthal distribution was constructed by starting with all events with M_w>6 and adding non-overlapping events down to M_w 5.4 at undersampled azimuths. We performed visual quality control on all waveforms. Helmholtz-corrected phase velocity maps were calculated from 20 to 100 seconds period using the Automated Surface-Wave Measurement System (ASWMS) (Jin & Gaherty, 2015; F.-C. Lin et al., 2009; F.-C. Lin & Ritzwoller, 2011) (Figure S3). The minimum inter-station distance for calculating cross-correlations was set to 50 km, and the maximum distance was varied with period such that it did not exceed ~4 wavelengths. The bandwidth range for the Gaussian filters applied to the waveform cross-correlations was 0.04-0.07 Hz. Automated quality controls based on the fraction of good measurements per event were intentionally relaxed for stations in the CRSP temporary network to obtain adequate data coverage near the Chile Triple Junction, and the larger velocity uncertainties near the triple junction at short periods reflect this choice.

Phase velocity dispersion curves from 8 to 100 seconds were constructed by combining the results from ambient noise and earthquake tomography (Figure S4). We used linear weighting across the overlapping periods, with ambient noise velocities weighted more at shorter periods and earthquake results at longer periods.

2.2 P receiver functions

We selected events 30-90° away from our study area with M_w>5.1 and a signal-to-noise ratio greater than 3 on the vertical component for the receiver function (RF) calculation. The seismograms were filtered from 0.33-1 Hz, and P first arrival picks were refined using STA/LTA (Withers et al., 1998) in a time window around the predicted onset time from the global model IASP91 (Kennett & Engdahl, 1991). P-to-s RFs were then calculated using the multitaper deconvolution method (Helffrich, 2006; Park et al., 1987; Park & Levin, 2000; Shibutani et al., 2008) and corrected for moveout using IASP91. For each station, a composite RF with uncertainties was obtained by taking the zeroth order component from harmonic decomposition (Bianchi et al., 2010). If azimuthal coverage was not sufficient to fit harmonics, the station average RF was used instead.

2.3 Bayesian inversion for velocity-depth models

We inverted for 1D velocity-depth models using a Markov chain Monte Carlo (MCMC) method (Shen et al., 2013). Each velocity-depth model was described by 14 parameters: layer thicknesses for sediments and crust; top and bottom velocities for the sediment layer; four cubic basis spline coefficients for crustal velocities; and six cubic basis spline coefficients for mantle velocities (Table S1). The total model depth was fixed at 300 km, with the lowermost 100 km of the model gradually converging to the global model AK135 (Kennett et al., 1995) since the data provide no constraints at these depths.

Initial prior distributions for the sediment and crustal layer thicknesses were set based on RFs. We used bootstrap stacking of H-k stacks to estimate an initial Moho depth for each station (Sandvol et al., 1998; Zhu & Kanamori, 2000). For sediment thickness, we performed a K-means clustering analysis (Pedregosa et al., 2011) on the first six seconds of the RF stacks for the stations, and used the clusters to divide the stations into those overlying “thick” sediments and “thin” sediments. The “thick” sediment cluster agreed well with the mapped extent of the Austral-Magallanes Basin (Cuitiño et al., 2019). For stations overlying “thick” sediment, the prior distribution for sediment thickness was set to 4 ± 4 km, and for stations with “thin” sediment the thickness prior distribution was set to 1 ± 1 km.

Prior distributions for velocities in all layers were set to typical values with large search ranges to allow for variation (Table S1). The sixth mantle spline coefficient at the base of our model was fixed at 4.7 km/s based on AK135, since the data have almost no sensitivity at 300 km depth.

We imposed some velocity constraints to ensure that accepted models were physically reasonable: all velocity parameters were less than 4.9 km/s, crustal velocities were less than 4.2 km/s, the velocity jump across the Moho was less than 0.7 km/s, and velocities were not allowed to decrease with depth through the sediments and crust. Dispersion curves and receiver functions were weighted equally in the joint misfit function after normalizing their respective uncertainties. We used 15 chains of 5000 steps each for the MCMC calculation. The posterior distributions for the 14 model parameters were calculated from the set of accepted models based on the misfit function (Shen et al., 2013) (Figure S5).

Inversions were first done for station locations. Prior distributions for the sediment and crustal layer thicknesses were then adjusted in places where the inversion failed to find a well-fitted model. This was particularly important for stations within the Austral-Magallanes Basin,

where the thick sediments violated the H-k stacking assumption of a constant-velocity crustal layer. We then inverted dispersion curves alone for velocity-depth model at grid points set at 0.3° intervals throughout the study area, using smoothed maps of crustal and sediment thicknesses from the station inversions to set layer thickness prior distributions.

The grid point and station results were combined by averaging together the 14 model parameters for each grid point with those for any stations within a 50 km radius. Weights for the station parameters were calculated based on proximity to the grid point. The model was smoothed laterally at each depth using a Gaussian filter with a standard deviation equal to the grid spacing.

2.4 Mantle viscosity calculation

Although there is no direct relationship between seismic velocity and mantle viscosity, velocity is commonly used to indirectly estimate viscosity since both are largely controlled by temperature. Mantle viscosities were estimated based on differences between our velocity model and V_{sv} from the global 1D model STW105 (Kustowski et al., 2008). The seismic anomalies were used to estimate temperature anomalies relative to a global average temperature model, which were then used along with experimentally-derived flow laws to estimate deviations from a global 1D viscosity model (Ivins et al., 2021; Wu et al., 2013). We used rheologic parameters for dry diffusion creep of olivine (Hirth & Kohlstedt, 2003; Karato, 2008), a reference mantle viscosity from IJ05-R2 (Ivins et al., 2013), and temperature derivatives that included both anharmonic and anelastic contributions (Karato, 2008). The calculated viscosities would not be significantly different for wet diffusion creep given parameter uncertainties (Hirth & Kohlstedt, 2003). The reference global average temperatures were calculated by proportionally weighting continental average geotherms (Stacey & Davis, 2008) and adiabatic temperature gradients beneath oceanic regions, giving 1486 K at 100 km, and 1582 K at 150 km. We set the fraction of the velocity anomaly attributed to temperature to 0.65, as found in a geodetic study of North America and Fennoscandia (Wu et al., 2013). While this temperature fraction may be different in Patagonia compared to stable cratonic regions, such variation would not change the pattern of relative viscosity differences across Patagonia. The remaining velocity anomaly is attributed to compositional variations in the mantle.

3 Results

3.1 Extent of the Patagonian slab window

Mantle velocities are low throughout the inferred slab window region, with a minimum velocity less than 4.1 km/s at 50 km depth, ~8% slower than the global average given by STW105 (Kustowski et al., 2008). The most intense portion of the shallow slow anomaly is north of 49°S, in the youngest part of the slab window (Figure 2). North of 51°S, the western edge of the anomaly at 100 km depth aligns with estimates of the extent of the subducting Antarctic slab from plate kinematic reconstructions (Breitsprecher & Thorkelson, 2009) and the trend of adakitic volcanism along the Austral Andes Volcanic Arc (Figure 2). Increased velocities north of Tierra del Fuego delineate the southeastern extent of the slab window effects and are consistent with xenolith studies suggesting the presence of a continental lithospheric block with thicker lithosphere (Schilling et al., 2017).

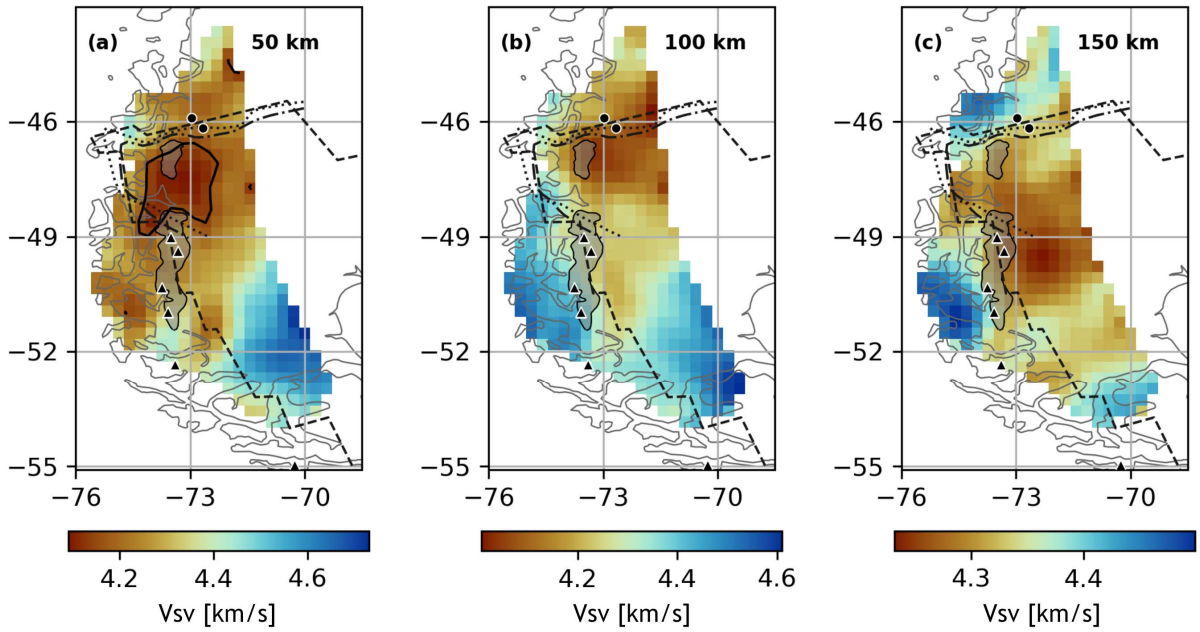

Figure 2: Velocity-depth slices. Maps show V_{sv} in km/s: **(a)** 50 km depth, contour at 4.15 km/s (solid black line); **(b)** 100 km depth; **(c)** 150 km depth. Other lines and symbols are as in Figure 1. Velocity uncertainties are ~0.1 km/s across most of the maps; velocity uncertainty maps are shown in Figure S6.

3.2 Thermal erosion of the South American lithosphere

Velocities directly beneath the crust near the CTJ are much lower than expected for continental lithosphere (4.1 km/s at 50 km, compared to 4.5 km/s for STW105; Kustowski et al., 2008), indicating that the lithospheric mantle is missing in the youngest part of the slab window (Figure 2a). Vertical cross sections through the slab window show that anomalously slow mantle velocities are present immediately below the Moho, with thin (<10 km thick) patches of faster mantle material at the Moho in places (Figure 3a, 45 to 47ºS).

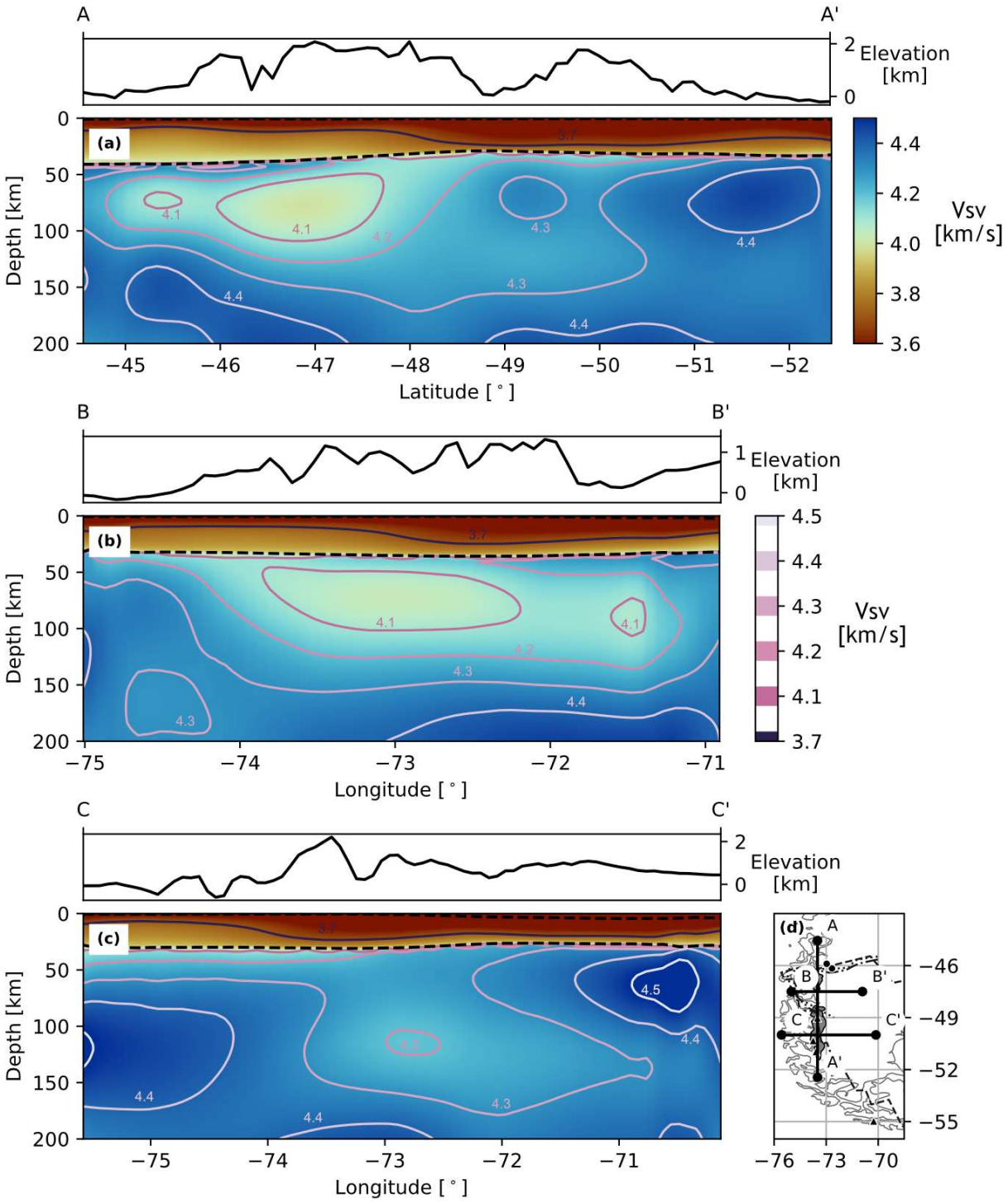

Figure 3: Velocity cross sections. Cross sections show V_{sv} along **(a)** 73.5°W, **(b)** 47.5°S, and **(c)** 50°S, with transect locations shown on a map **(d)**. Other lines and symbols on the map are as in Figure 1. Topography over each transect is plotted above the velocities (Ryan et al., 2009). Dashed black lines mark the base of the sediments and the Moho on each cross section, and

labeled lines show isovelocity contours. The V_{sv} color scale is saturated at 3.6 km/s on the low end to emphasize slow anomalies in the mantle.

The absence of lithospheric mantle near the CTJ suggests that mantle dynamics associated with the slab window have eroded the base of the plate. Thermal erosion of the overriding plate is predicted by thermo-mechanical models of ridge subduction (Groome & Thorkelson, 2009), and shallow slow velocity anomalies beneath the Antarctic Peninsula have been similarly interpreted (Lloyd et al., 2020). Previous studies have inferred that the Patagonian lithosphere has thinned above the slab window based on regional heat flow data (Ávila & Dávila, 2018), crustal thickness measurements (Robertson Maurice et al., 2003), and GIA models fit to observed uplift rates (Lange et al., 2014; Richter et al., 2016).

The process of thermal erosion likely requires the presence of melt or fluids, as purely conductive heating is too slow relative to the age of the slab window. In the absence of a present-day slab and slab-derived volatiles, melt may be supplied by decompression of upwelling asthenospheric mantle. There are no known active Holocene volcanos over the slowest part of the velocity anomaly, but the presence of the icefields complicates the mapping of volcanic activity. Shear wave splitting analyses show a strong E–W fast direction near the CTJ, indicating vigorous mantle flow around the edge of the Nazca slab (Russo, Gallego, et al., 2010; Russo, VanDecar, et al., 2010; Wiens et al., 2021), and fast mantle flow in the shallow asthenosphere may assist in the removal of lithospheric material.

Lithospheric erosion near the CTJ contrasts with the structure farther south, where fast velocities indicate that the lithospheric mantle is largely intact beneath the Austral-Magallanes Basin. Patagonia has a complex history of terrane accretion (Ramos & Ghiglione, 2008), and it is possible that the lithosphere in the south was thicker prior to the opening of the slab window. Alternatively, thermal erosion may have been less efficient during the earliest stages of ridge subduction, becoming more efficient over time as the slab window thermally perturbed the surrounding mantle. As ridge subduction initiated only 18 Ma and subsequent ridge segments entered the trench at ~12 Ma, 6 Ma, and 3 Ma, we expect that timescales of conductive cooling are too short relative to the age of the slab window to allow for significant re-formation of mantle lithosphere even in the oldest parts of the window (Boutonnet et al., 2010).

The crust thins by >10 km from north to south over the slab window (Figure 3, S7, S8). This trend is opposite the lithospheric erosion seen at the Moho, and is unlikely to be entirely due to surface erosion since the thinning is not primarily in the upper crust. Along the west coast of North America, the passage of the migrating Mendocino Triple Junction is thought to have caused rapid, temporary crustal thickening followed by crustal thinning (Furlong & Govers, 1999). The same mechanism may be at work in Patagonia, but the trend of mean relief along the Austral Andes does not match predictions for flexural downwarping associated with this model for crustal modification (Georgieva et al., 2016). Preexisting structure, overthrusting of terranes, thermal erosion, and tectonic extension have also been proposed to explain crustal structure near the CTJ (Rodriguez & Russo, 2020), and further measurements extending north of our study region would help clarify the source of the variations in crustal thickness.

4 Implications for glacial isostatic adjustment

Mantle viscosity structure strongly controls GIA, which in turn responds to spatial and temporal ice-mass variations. High geodetic uplift rates around the NPI and SPI (≥4 cm/yr) have

been attributed to anomalous mantle viscosities lower than $2x10^{18}$ Pa s (Ivins & James, 2004; Lange et al., 2014; Richter et al., 2016), and recent GIA models suggest that reproducing observed uplift rates requires either mantle viscosities that are significantly lower beneath the NPI compared to the SPI or more ice mass loss in the NPI than previously estimated (Lange et al., 2014; Russo et al., 2021). The observed location of the slowest part of the seismic velocity anomaly north of 49°S is consistent with the former explanation, and viscosities estimated from our velocity model also point to both low overall viscosity in the slab window and a difference in structure beneath the two icefields (Figure 4). Our estimated viscosities are mostly higher than the values obtained by previous geodetic studies (Lange et al., 2014; Richter et al., 2016), but we emphasize that the absolute viscosity values we obtain are highly sensitive to uncertain parameters such as the fraction of velocity variation due to temperature. The extent of the slow anomaly also suggests that gradients in uplift rates along the SPI may reflect latitudinal variation in mantle viscosity. In broader terms, the strong lateral heterogeneity in mantle viscosity indicated by the velocity model implies that the geodetic response to glacial unloading in Patagonia will be highly three-dimensional, and cannot be fully described by symmetric deformation predicted for a radially layered mantle, particularly with respect to the prediction of horizontal crustal motions (Klemann et al., 2007).

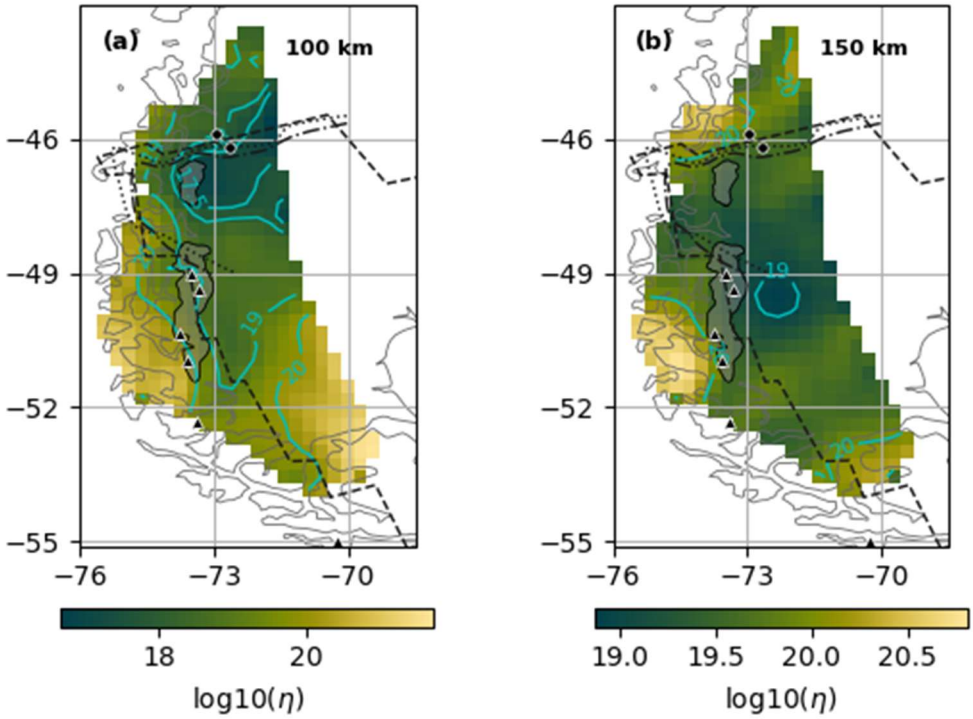

Figure 4: Estimated mantle viscosity based on the seismic velocity model. Maps of $\log_{10}(\eta)$ at **(a)** 100 km and **(b)** 150 km depth. Other lines and symbols on the map are as described in the captions for Figures 1 and 2.

The patterns of lithospheric erosion and thinning observed in our velocity model are also expected to affect GIA. While the seismic lithosphere is not exactly equivalent to the elastic lithosphere relevant to geodetic models, both terms refer to a layer of colder, more rigid material

that acts as a lowpass filter on the response of the mantle to changes in surface loading. The thin lithosphere observed near the CTJ enables shorter wavelength signals from GIA loading and mantle viscosity variations to be observed in surface deformation and topography. In the south, the fast velocities to the east indicate that thicker continental lithospheric mantle beneath the Austral-Magallanes Basin may constrain mantle flow patterns in the older parts of the slab window by blocking shallow latitudinal flow (Klemann et al., 2007). In this scenario, horizontal surface motions on the eastern side of the SPI are predicted to be dominantly to the east, and GNSS observations of horizontal surface displacements support this prediction where data are available along the eastern side of the northern SPI (Richter et al., 2016).

Quantifying ice mass changes on the Patagonian Icefields is crucial for projecting future water resources and informing models of global sea level rise. Temperate mountain glaciers including the NPI and SPI currently contribute substantially to global mean sea level rise (Jacob et al., 2012; Radić & Hock, 2011). Ice and hydrological mass changes are efficiently monitored by satellite gravimetry, provided the GIA gravity effect is accurately removed (Ivins et al., 2011). However, there are large trade-offs in GIA modeling between ice mass history and mantle viscosity structure (Lange et al., 2014), so uncertainties in mantle viscosity propagate forward into highly uncertain ice mass change rates (Richter et al., 2019). Constraining the regional 3D viscosity structure provides the space gravimetry community with key information on the solid Earth contribution to the secular mass change signal in Patagonia.

The geologically rapid response of Patagonian topography to ice mass changes makes the area above the slab window ideal for studying the connections between the solid Earth rheology and dynamics, surface processes, and climate. The heterogeneous mantle structure indicated by seismic velocities implies that the isostatic response to ice mass changes will also be heterogeneous, and the absence of mantle lithosphere over the slab window promotes the observation of shorter wavelength variations in surface deformation. Lateral heterogeneity in mantle viscosity and lithospheric thickness, guided by seismic models and other geophysical observations, must be incorporated into GIA modeling in this region. The resulting higher quality models will help advance our understanding of the history and the future of the cryosphere and hydrosphere in Patagonia.

Acknowledgments

We thank Patrick Shore, Gerardo Connon, Leticia Duca, Celeste Bollini, Nora Sabbione, Gerd Sielfeld, Daniel Valladares, and many others for their work in planning, deploying, servicing, and recovering the GUANACO seismic array. We also thank Maeva Pourpoint for her work in the field and with initial data processing; Weisen Shen for sharing his Bayesian inversion code; and Zhengyang Zhou and Zongshan Li for their help with several of the software packages used for data processing. We thank reviewers R. M. Russo and Volker Klemann for their thoughtful comments. The OCCAP Foundation assisted in arranging boat transport to remote stations in Chile. ENAP Magallanes provided additional seismic data. The seismic instruments were provided by the IRIS-PASSCAL Instrument Center at New Mexico Tech. The facilities of the IRIS Consortium are supported by the National Science Foundation's SAGE Award under Cooperative Support Agreement EAR-1851048. The GUANACO project is funded by the National Science Foundation under grants EAR-1714154 to WUSTL and EAR-1714662 to SMU, and E. R. I. was supported by NASA under grant NNH19ZDA001N-GRACEFO.

Open Research

Data used in this study is from the GUANACO, SEPA, and CRSP temporary seismic networks (network codes: 1P, 10/2018-03/2021; XB, 02/1997-10/1998; YJ, 12/2004-12/2006), permanent stations from the Chile Network, GEOSCOPE, and the Antarctic Seismographic Argentinian Italian Network (network codes: C, C1, G, AI), and stations operated and maintained by ENAP. Data for all except the ENAP stations can be obtained from the IRIS DMC (https://ds.iris.edu/ds/nodes/dmc). The earthquake records and ambient noise cross-correlations for ENAP stations used in this study are publicly available (Mark et al., 2021a, https://doi.org/10.5281/zenodo.5508198). The final velocity and viscosity models presented in this paper are also available (Mark et al., 2021b, https://doi.org/10.5281/zenodo.5794167).

Publicly released versions of the codes used for analysis can be found at: https://github.com/NoiseCIEI/Seed2Cor, https://github.com/NoiseCIEI/AFTAN, https://github.com/NoiseCIEI/RayTomo, https://github.com/trichter/rf, https://github.com/jinwar/matgsdf, and http://diapiro.ictja.csic.es/gt/mschi/SCIENCE/tseries.html#software. These codes are currently only available on github and researchers' personal websites. Color palettes for all figures are from Fabio Crameri's ScientificColourMaps7 (https://doi.org/10.5281/zenodo.1243862).

References

Agurto-Detzel, H., Rietbrock, A., Bataille, K., Miller, M., Iwamori, H., & Priestley, K. (2014). Seismicity distribution in the vicinity of the Chile Triple Junction, Aysén Region, southern Chile. *Journal of South American Earth Sciences*, *51*, 1–11. https://doi.org/10.1016/j.jsames.2013.12.011

Ávila, P., & Dávila, F. M. (2018). Heat flow and lithospheric thickness analysis in the Patagonian asthenospheric windows, southern South America. *Tectonophysics*, *747–748*, 99–107. https://doi.org/10.1016/j.tecto.2018.10.006

Barmin, M. P., Ritzwoller, M. H., & Levshin, A. L. (2001). A Fast and Reliable Method for Surface Wave Tomography. *Pure Appl. Geophys.*, *158*, 25.

Bensen, G. D., Ritzwoller, M. H., Barmin, M. P., Levshin, A. L., Lin, F., Moschetti, M. P., et al. (2007). Processing seismic ambient noise data to obtain reliable broad-band surface wave dispersion measurements. *Geophysical Journal International*, *169*(3), 1239–1260. https://doi.org/10.1111/j.1365-246X.2007.03374.x

Bianchi, I., Park, J., Piana Agostinetti, N., & Levin, V. (2010). Mapping seismic anisotropy using harmonic decomposition of receiver functions: An application to Northern Apennines, Italy. *Journal of Geophysical Research*, *115*(B12), B12317. https://doi.org/10.1029/2009JB007061

Bourgois, J., Lagabrielle, Y., Martin, H., Dyment, J., Frutos, J., & Cisternas, M. E. (2016). A Review on Forearc Ophiolite Obduction, Adakite-Like Generation, and Slab Window Development at the Chile Triple Junction Area: Uniformitarian Framework for Spreading-Ridge Subduction. *Pure and Applied Geophysics*, *173*(10–11), 3217–3246. https://doi.org/10.1007/s00024-016-1317-9

Boutonnet, E., Arnaud, N., Guivel, C., Lagabrielle, Y., Scalabrino, B., & Espinoza, F. (2010). Subduction of the South Chile active spreading ridge: A 17Ma to 3Ma magmatic record

in central Patagonia (western edge of Meseta del Lago Buenos Aires, Argentina). *Journal of Volcanology and Geothermal Research*, *189*(3–4), 319–339. https://doi.org/10.1016/j.jvolgeores.2009.11.022

Breitsprecher, K., & Thorkelson, D. J. (2009). Neogene kinematic history of Nazca–Antarctic–Phoenix slab windows beneath Patagonia and the Antarctic Peninsula. *Tectonophysics*, *464*(1–4), 10–20. https://doi.org/10.1016/j.tecto.2008.02.013

Cande, S. C., Leslie, R. B., Parra, J. C., & Hobart, M. (1987). Interaction between the Chile Ridge and Chile Trench: Geophysical and geothermal evidence. *Journal of Geophysical Research*, *92*(B1), 495. https://doi.org/10.1029/JB092iB01p00495

Cuitiño, J. I., Varela, A. N., Ghiglione, M. C., Richiano, S., & Poiré, D. G. (2019). The Austral-Magallanes Basin (Southern Patagonia): A Synthesis of its Stratigraphy and Evolution. *Latin American Journal of Sedimentology and Basin Analysis*, *26*(2), 12.

Davies, B., Darvill, C., Lovell, H., Bendle, J., Dowdeswell, J., Fabel, D., et al. (2020). Data for: The evolution of the Patagonian Ice Sheet from 35 ka to the Present Day (PATICE), *1*. https://doi.org/10.17632/ztz59y79vv.1

DeLong, S. E., Schwarz, W. M., & Anderson, R. N. (1979). Thermal effects of ridge subduction. *Earth and Planetary Science Letters*, *44*(2), 239–246. https://doi.org/10.1016/0012-821X(79)90172-9

Dickinson, W. R. (1981). Plate tectonics of the continental margin of California. In W. G. Ernst (Ed.), *The Geotectonic Development of California (Rubey)* (Vol. 1, pp. 1–28). Prentice Hall.

Dietrich, R., Ivins, E. R., Casassa, G., Lange, H., Wendt, J., & Fritsche, M. (2010). Rapid crustal uplift in Patagonia due to enhanced ice loss. *Earth and Planetary Science Letters*, *289*(1–2), 22–29. https://doi.org/10.1016/j.epsl.2009.10.021

Forsythe, R. D., Nelson, E. P., Carr, M. J., Kaeding, M. E., Herve, M., Mpodozis, C., et al. (1986). Pliocene near-trench magmatism in southern Chile: A possible manifestation of ridge collision. *Geology*, *14*, 5.

Furlong, K. P., & Govers, R. (1999). Ephemeral crustal thickening at a triple junction: The Mendocino crustal conveyor. *Geology*, *27*(2), 4.

Gallego, A., Russo, R. M., Comte, D., Mocanu, V. I., Murdie, R. E., & Vandecar, J. C. (2010). Seismic noise tomography in the Chile ridge subduction region. *Geophysical Journal International*, *182*(3), 1478–1492. https://doi.org/10.1111/j.1365-246X.2010.04691.x

Georgieva, V., Melnick, D., Schildgen, T. F., Ehlers, T. A., Lagabrielle, Y., Enkelmann, E., & Strecker, M. R. (2016). Tectonic control on rock uplift, exhumation, and topography above an oceanic ridge collision: Southern Patagonian Andes (47°S), Chile: Neotectonics and Topography in Patagonia. *Tectonics*, *35*(6), 1317–1341. https://doi.org/10.1002/2016TC004120

Gorring, M. L., Kay, S. M., Zeitler, P. K., Ramos, V. A., Rubiolo, D., Fernandez, M. I., & Panza, J. L. (1997). Neogene Patagonian plateau lavas: Continental magmas associated with ridge collision at the Chile Triple Junction. *Tectonics*, *16*(1), 1–17. https://doi.org/10.1029/96TC03368

Groome, W. G., & Thorkelson, D. J. (2009). The three-dimensional thermo-mechanical signature of ridge subduction and slab window migration. *Tectonophysics*, *464*(1–4), 70–83. https://doi.org/10.1016/j.tecto.2008.07.003

Guillaume, B., Martinod, J., Husson, L., Roddaz, M., & Riquelme, R. (2009). Neogene uplift of central eastern Patagonia: Dynamic response to active spreading ridge subduction? *Tectonics*, *28*(2). https://doi.org/10.1029/2008TC002324

Guivel, C., Lagabrielle, Y., Bourgois, J., Martin, H., Arnaud, N., Fourcade, S., et al. (2003). Very shallow melting of oceanic crust during spreading ridge subduction: Origin of near-trench Quaternary volcanism at the Chile Triple Junction. *Journal of Geophysical Research: Solid Earth*, *108*(B7). https://doi.org/10.1029/2002JB002119

Helffrich, G. (2006). Extended-Time Multitaper Frequency Domain Cross-Correlation Receiver-Function Estimation. *Bulletin of the Seismological Society of America*, *96*(1), 344–347. https://doi.org/10.1785/0120050098

Hirth, G., & Kohlstedt, D. (2003). Rheology of the Upper Mantle and the Mantle Wedge: A View from the Experimentalists. In J. Eiler (Ed.), *Inside the Subduction Factory* (pp. 83–105). American Geophysical Union. https://doi.org/10.1029/138GM06

Ivins, E. R., & James, T. S. (2004). Bedrock response to Llanquihue Holocene and present-day glaciation in southernmost South America. *Geophysical Research Letters*, *31*(24), L24613. https://doi.org/10.1029/2004GL021500

Ivins, E. R., Watkins, M. M., Yuan, D.-N., Dietrich, R., Casassa, G., & Rülke, A. (2011). On-land ice loss and glacial isostatic adjustment at the Drake Passage: 2003–2009. *Journal of Geophysical Research*, *116*(B2), B02403. https://doi.org/10.1029/2010JB007607

Ivins, E. R., James, T. S., Wahr, J., O. Schrama, E. J., Landerer, F. W., & Simon, K. M. (2013). Antarctic contribution to sea level rise observed by GRACE with improved GIA correction. *Journal of Geophysical Research: Solid Earth*, *118*(6), 3126–3141. https://doi.org/10.1002/jgrb.50208

Ivins, E. R., Wal, W. van der, Wiens, D. A., Lloyd, A. J., & Caron, L. (2021). Antarctic Upper Mantle Rheology. *Geological Society, London, Memoirs*, *56*. https://doi.org/10.1144/M56-2020-19

Jacob, T., Wahr, J., Pfeffer, W. T., & Swenson, S. (2012). Recent contributions of glaciers and ice caps to sea level rise. *Nature*, *482*(7386), 514–518. https://doi.org/10.1038/nature10847

Jin, G., & Gaherty, J. B. (2015). Surface wave phase-velocity tomography based on multichannel cross-correlation. *Geophysical Journal International*, 16.

Karato, S. (2008). Deformation of earth materials. *An Introduction to the Rheology of Solid Earth*, *463*.

Kennett, B. L. N., & Engdahl, E. R. (1991). Traveltimes for global earthquake location and phase identification. *Geophysical Journal International*, *105*(2), 429–465. https://doi.org/10.1111/j.1365-246X.1991.tb06724.x

Kennett, B. L. N., Engdahl, E. R., & Buland, R. (1995). Constraints on seismic velocities in the Earth from traveltimes. *Geophysical Journal International*, *122*(1), 108–124.

Klemann, V., Ivins, E. R., Martinec, Z., & Wolf, D. (2007). Models of active glacial isostasy roofing warm subduction: Case of the South Patagonian Ice Field. *Journal of Geophysical Research*, *112*(B9), B09405. https://doi.org/10.1029/2006JB004818

Kustowski, B., Ekström, G., & Dziewoński, A. M. (2008). Anisotropic shear-wave velocity structure of the Earth's mantle: A global model. *Journal of Geophysical Research*, *113*(B6), B06306. https://doi.org/10.1029/2007JB005169

Lange, H., Casassa, G., Ivins, E. R., Schröder, L., Fritsche, M., Richter, A., et al. (2014). Observed crustal uplift near the Southern Patagonian Icefield constrains improved viscoelastic Earth models. *Geophysical Research Letters*, *41*(3), 805–812. https://doi.org/10.1002/2013GL058419

Lin, F.-C., & Ritzwoller, M. H. (2011). Helmholtz surface wave tomography for isotropic and azimuthally anisotropic structure. *Geophysical Journal International*, *186*(3), 1104–1120. https://doi.org/10.1111/j.1365-246X.2011.05070.x

Lin, F.-C., Ritzwoller, M. H., & Snieder, R. (2009). Eikonal tomography: surface wave tomography by phase front tracking across a regional broad-band seismic array. *Geophysical Journal International*, *177*(3), 1091–1110. https://doi.org/10.1111/j.1365-246X.2009.04105.x

Lin, S. (2014). Three-dimensional mantle circulations and lateral slab deformation in the southern Chilean subduction zone. *Journal of Geophysical Research: Solid Earth*, *119*(4), 3879–3896. https://doi.org/10.1002/2013JB010864

Lloyd, A. J., Wiens, D. A., Zhu, H., Tromp, J., Nyblade, A. A., Aster, R. C., et al. (2020). Seismic Structure of the Antarctic Upper Mantle Imaged with Adjoint Tomography. *Journal of Geophysical Research: Solid Earth*, *125*(3), 2019JB017823. https://doi.org/10.1029/2019JB017823

Magnani, M. B., Ito, E., Wiens, D., Wickert, A. D., Ivins, E. R., Fedotova, A., et al. (2020). Solid Earth response of the Patagonian Andes to post-Little Ice Age glacial retreat: a multi-pronged approach. *AGU Fall Meeting Abstracts*, *2020*, G013-05.

Mark, H. F., Wiens, D. A., Ivins, E. R., Richter, A., Ben Mansour, W., Magnani, M. B., et al. (2021a). Earthquake records and ambient noise cross correlations from ENAP Magallanes seismographs, Jan 2019- Mar 2020 [Data set]. Zenodo. https://doi.org/10.5281/zenodo.5508198

Mark, H. F., Wiens, D. A., Ivins, E. R., Richter, A., Ben Mansour, W., Magnani, M. B., et al. (2021b). Velocity and viscosity models for southern Patagonia, from the GUANACO experiment [Data set]. Zenodo. https://doi.org/10.5281/zenodo.5794167

Marshak, R. S., & Karig, D. E. (1977). Triple junctions as a cause for anomalously near-trench igneous activity between the trench and volcanic arc. *Geology*, *5*(4), 233–236. https://doi.org/10.1130/0091-7613(1977)5<233:TJAACF>2.0.CO;2

McCrory, P. A., Wilson, D. S., & Stanley, R. G. (2009). Continuing evolution of the Pacific–Juan de Fuca–North America slab window system—A trench–ridge–transform example from the Pacific Rim. *Tectonophysics*, *464*(1–4), 30–42. https://doi.org/10.1016/j.tecto.2008.01.018

Murdie, R. E., & Russo, R. M. (1999). Seismic anisotropy in the region of the Chile margin triple junction. *Journal of South American Earth Sciences*, *12*(3), 261–270. https://doi.org/10.1016/S0895-9811(99)00018-8

Oerlemans, J. (2005). Extracting a Climate Signal from 169 Glacier Records. *Science*, *308*(5722), 675–677. https://doi.org/10.1126/science.1107046

Park, J., & Levin, V. (2000). Receiver Functions from Multiple-Taper Spectral Correlation Estimates. *Bulletin of the Seismological Society of America*, *90*(6), 1507–1520. https://doi.org/10.1785/0119990122

Park, J., Lindberg, C. R., & Vernon, F. L. (1987). Multitaper spectral analysis of high-frequency seismograms. *Journal of Geophysical Research: Solid Earth*, *92*(B12), 12675–12684. https://doi.org/10.1029/JB092iB12p12675

Pedregosa, F., Varoquaux, G., Gramfort, A., Michel, V., Thirion, B., Grisel, O., et al. (2011). Scikit-learn: Machine Learning in Python. *Journal of Machine Learning Research*, *12*, 2825–2830.

Radić, V., & Hock, R. (2011). Regionally differentiated contribution of mountain glaciers and ice caps to future sea-level rise. *Nature Geoscience*, *4*(2), 91–94. https://doi.org/10.1038/ngeo1052

Ramos, V. A., & Ghiglione, M. C. (2008). Tectonic Evolution of the Patagonian Andes. In *Developments in Quaternary Sciences* (Vol. 11, pp. 57–71). Elsevier. https://doi.org/10.1016/S1571-0866(07)10004-X

Richter, A., Ivins, E. R., Lange, H., Mendoza, L., Schröder, L., Hormaechea, J. L., et al. (2016). Crustal deformation across the Southern Patagonian Icefield observed by GNSS. *Earth and Planetary Science Letters*, *452*, 206–215. https://doi.org/10.1016/j.epsl.2016.07.042

Richter, A., Groh, A., Horwath, M., Ivins, E. R., Marderwald, E., Hormaechea, J. L., et al. (2019). The Rapid and Steady Mass Loss of the Patagonian Icefields throughout the GRACE Era: 2002–2017. *Remote Sensing*, *11*(8), 909. https://doi.org/10.3390/rs11080909

Robertson Maurice, S. D., Wiens, D. A., Koper, K. D., & Vera, E. (2003). Crustal and upper mantle structure of southernmost South America inferred from regional waveform inversion. *Journal of Geophysical Research: Solid Earth*, *108*(B1). https://doi.org/10.1029/2002JB001828

Rodriguez, E. E., & Russo, R. M. (2020). Southern Chile crustal structure from teleseismic receiver functions: Responses to ridge subduction and terrane assembly of Patagonia. *Geosphere*, *16*(1), 378–391. https://doi.org/10.1130/GES01692.1

Russo, R. M., Gallego, A., Comte, D., Mocanu, V. I., Murdie, R. E., & VanDecar, J. C. (2010). Source-side shear wave splitting and upper mantle flow in the Chile Ridge subduction region. *Geology*, *38*(8), 707–710. https://doi.org/10.1130/G30920.1

Russo, R. M., VanDecar, J. C., Comte, D., Mocanu, V. I., Gallego, A., & Murdie, R. E. (2010). Subduction of the Chile Ridge: Upper mantle structure and flow. *GSA Today*, 4–10. https://doi.org/10.1130/GSATG61A.1

Russo, R. M., Luo, H., Wang, K., Ambrosius, B., Mocanu, V., He, J., et al. (2021). Lateral variation in slab window viscosity inferred from global navigation satellite system (GNSS)–observed uplift due to recent mass loss at Patagonia ice fields. *Geology*. https://doi.org/10.1130/G49388.1

Ryan, W. B. F., Carbotte, S. M., Coplan, J. O., O'Hara, S., Melkonian, A., Arko, R., et al. (2009). Global Multi-Resolution Topography synthesis. *Geochemistry, Geophysics, Geosystems*, *10*(3), Q03014. https://doi.org/10.1029/2008GC002332

Sandvol, E., Seber, D., Calvert, A., & Barazangi, M. (1998). Grid search modeling of receiver functions: Implications for crustal structure in the Middle East and North Africa. *Journal of Geophysical Research: Solid Earth*, *103*(B11), 26899–26917. https://doi.org/10.1029/98JB02238

Schilling, M. E., Carlson, R. W., Tassara, A., Conceição, R. V., Bertotto, G. W., Vásquez, M., et al. (2017). The origin of Patagonia revealed by Re-Os systematics of mantle xenoliths. *Precambrian Research*, *294*, 15–32. https://doi.org/10.1016/j.precamres.2017.03.008

Schimmel, M., & Gallart, J. (2007). Frequency-dependent phase coherence for noise suppression in seismic array data. *Journal of Geophysical Research: Solid Earth*, *112*(B4). https://doi.org/10.1029/2006JB004680

Schimmel, M., Stutzmann, E., & Gallart, J. (2011). Using instantaneous phase coherence for signal extraction from ambient noise data at a local to a global scale: Ambient noise signal extraction. *Geophysical Journal International*, *184*(1), 494–506. https://doi.org/10.1111/j.1365-246X.2010.04861.x

Shen, W., Ritzwoller, M. H., Schulte-Pelkum, V., & Lin, F.-C. (2013). Joint inversion of surface wave dispersion and receiver functions: a Bayesian Monte-Carlo approach. *Geophysical Journal International*, *192*(2), 807–836. https://doi.org/10.1093/gji/ggs050

Shen, W., Ritzwoller, M. H., Kang, D., Kim, Y., Lin, F.-C., Ning, J., et al. (2016). A seismic reference model for the crust and uppermost mantle beneath China from surface wave dispersion. *Geophysical Journal International*, *206*(2), 954–979. https://doi.org/10.1093/gji/ggw175

Shibutani, T., Ueno, T., & Hirahara, K. (2008). Improvement in the Extended-Time Multitaper Receiver Function Estimation Technique. *Bulletin of the Seismological Society of America*, *98*(2), 812–816. https://doi.org/10.1785/0120070226

Stacey, F. D., & Davis, P. M. (2008). *Physics of the Earth*. Cambridge University Press.

Stern, C. R., & Kilian, R. (1996). Role of the subducted slab, mantle wedge and continental crust in the generation of adakites from the Andean Austral Volcanic Zone. *Contributions to Mineralogy and Petrology*, *123*(3), 263–281. https://doi.org/10.1007/s004100050155

Thorkelson, D. J. (1996). Subduction of diverging plates and the principles of slab window formation. *Tectonophysics*, *255*(1–2), 47–63. https://doi.org/10.1016/0040-1951(95)00106-9

Thorkelson, D. J., & Breitsprecher, K. (2005). Partial melting of slab window margins: genesis of adakitic and non-adakitic magmas. *Lithos*, *79*(1–2), 25–41. https://doi.org/10.1016/j.lithos.2004.04.049

Wiens, D. A., Robertson, S., Smith, G. P., Shore, P., Vera, E., Barrientos, S., et al. (1998). Seismic Experiment in Patagonia and Antarctica (SEPA). *IRIS Newsletter*, *17*(1), 9–11.

Wiens, D. A., Mansour, W. B., Mark, H. F., Shore, P., Richter, A., & Barrientos, S. (2021). Geodynamics of the Patagonian Slab Window constrained by Shear Wave Splitting and Seismic Imaging. Presented at the AGU Fall Meeting, Earth and Space Science Open Archive. https://doi.org/10.1002/essoar.10509443.1

Withers, M., Aster, R., Young, C., Beiriger, J., Harris, M., Moore, S., & Trujillo, J. (1998). A Comparison of Select Trigger Algorithms for Automated Global Seismic Phase and Event Detection. *Bulletin of the Seismological Society of America*, *88*(1), 12.

Wu, P., Wang, H., & Steffen, H. (2013). The role of thermal effect on mantle seismic anomalies under Laurentia and Fennoscandia from observations of Glacial Isostatic Adjustment. *Geophysical Journal International*, *192*(1), 7–17. https://doi.org/10.1093/gji/ggs009

Zhu, L., & Kanamori, H. (2000). Moho depth variation in southern California from teleseismic receiver functions. *Journal of Geophysical Research: Solid Earth*, *105*(B2), 2969–2980. https://doi.org/10.1029/1999JB900322

Geophysical Research Letters

Supporting Information for

Lithospheric Erosion in the Patagonian Slab Window, and Implications for Glacial Isostasy

Hannah F. Mark[1], Douglas A. Wiens[1], Erik R. Ivins[2], Andreas Richter[3], Walid Ben Mansour[1], M. Beatrice Magnani[4], Eric Marderwald[3], Rodrigo Adaros[5], Sergio Barrientos[6]

[1]Department of Earth and Planetary Sciences, Washington University in St. Louis; [2]Jet Propulsion Laboratory, California Institute of Technology; [3]Laboratorio MAGGIA, Universidad Nacional de La Plata; CONICET; [4]Southern Methodist University; [5]Empresa Nacional del Petróleo, Magallanes; [6]Centro Sismológico Nacional, Universidad de Chile

Contents of this file

Introduction

This file contains supplemental figures and a table detailing parameters used for Bayesian inversion.

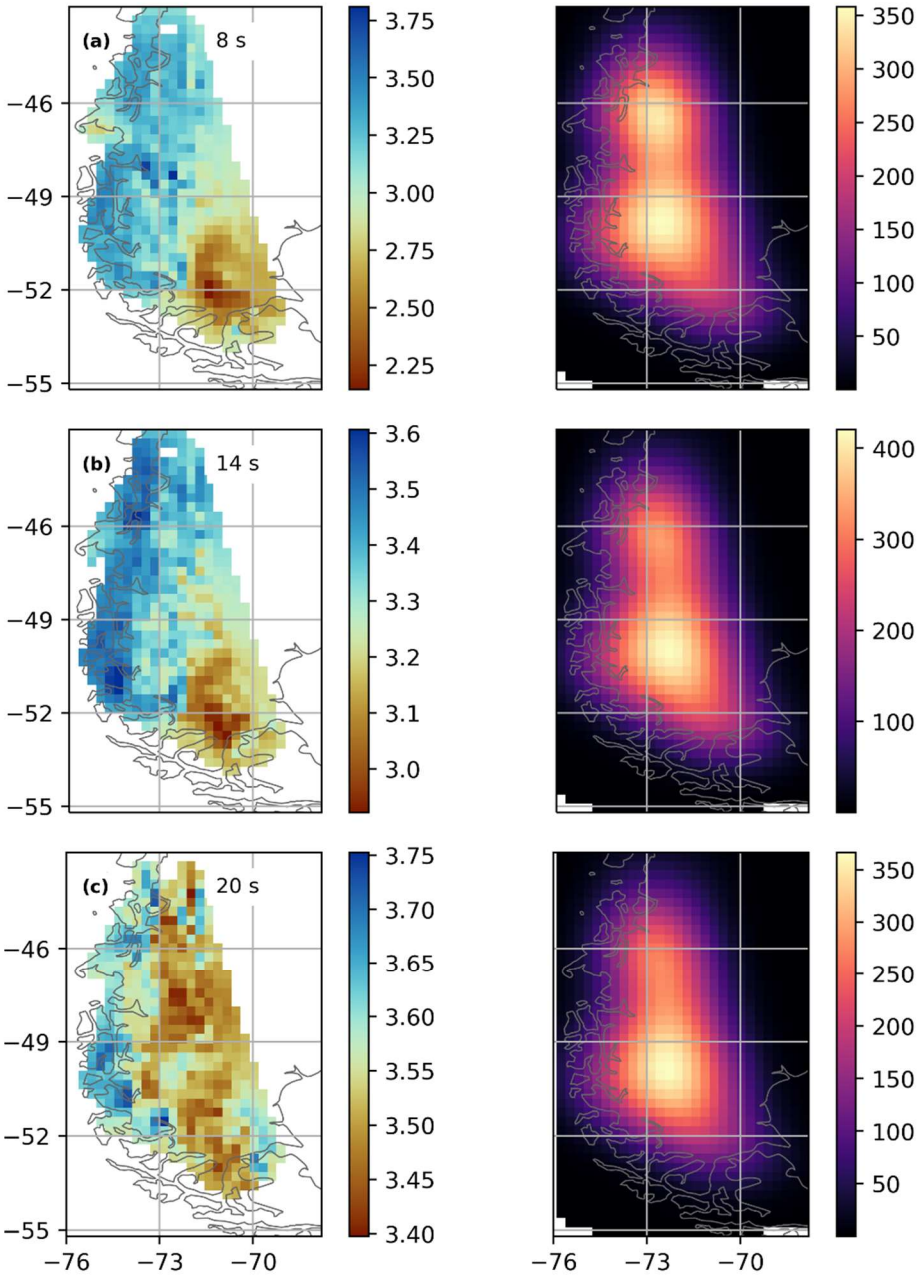

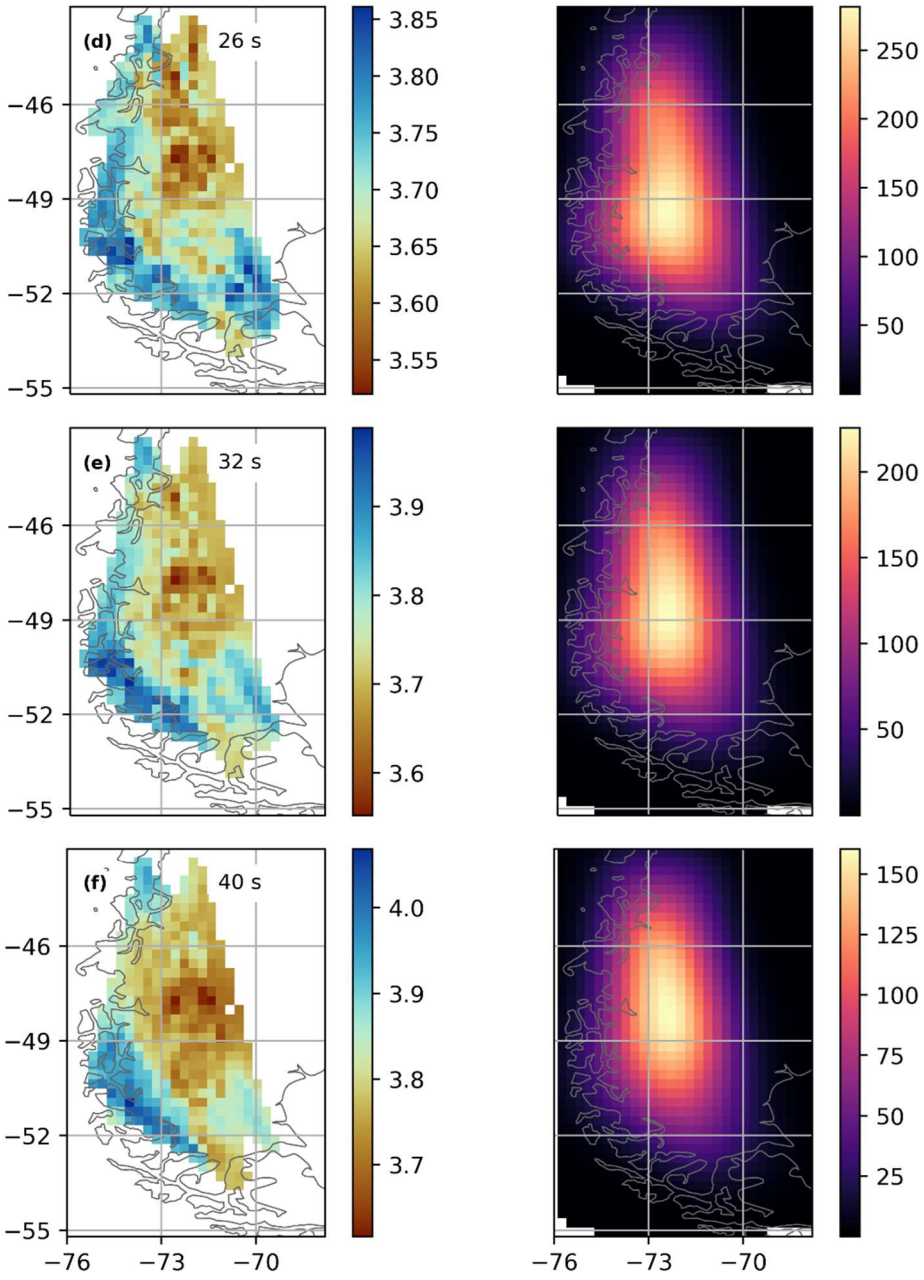

Figure S1. Phase velocity maps from ambient noise tomography. The left column shows phase velocities in km/s, and the right column shows path density smoothed over the map. Phase velocities are shown at periods of **(a)** 8 seconds, **(b)** 14 seconds, **(c)** 20 seconds, **(d)** 26 seconds, **(e)** 32 seconds, and **(f)** 40 seconds. Velocities are only shown where path density is greater than 10 and the resolution length scale is greater than 0.02.

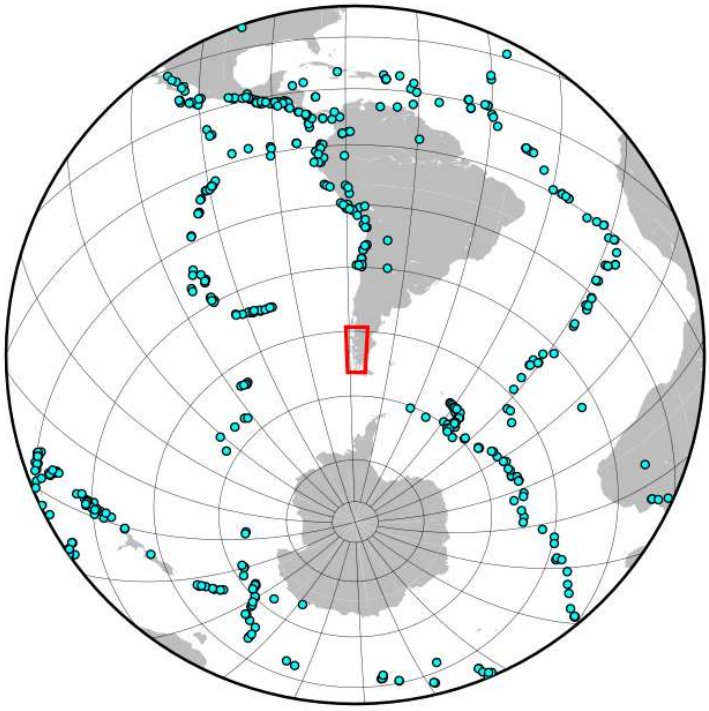

Figure S2. Event distribution map. Blue dots mark the locations of earthquakes used for tomography. The study region is outlined by a red box.

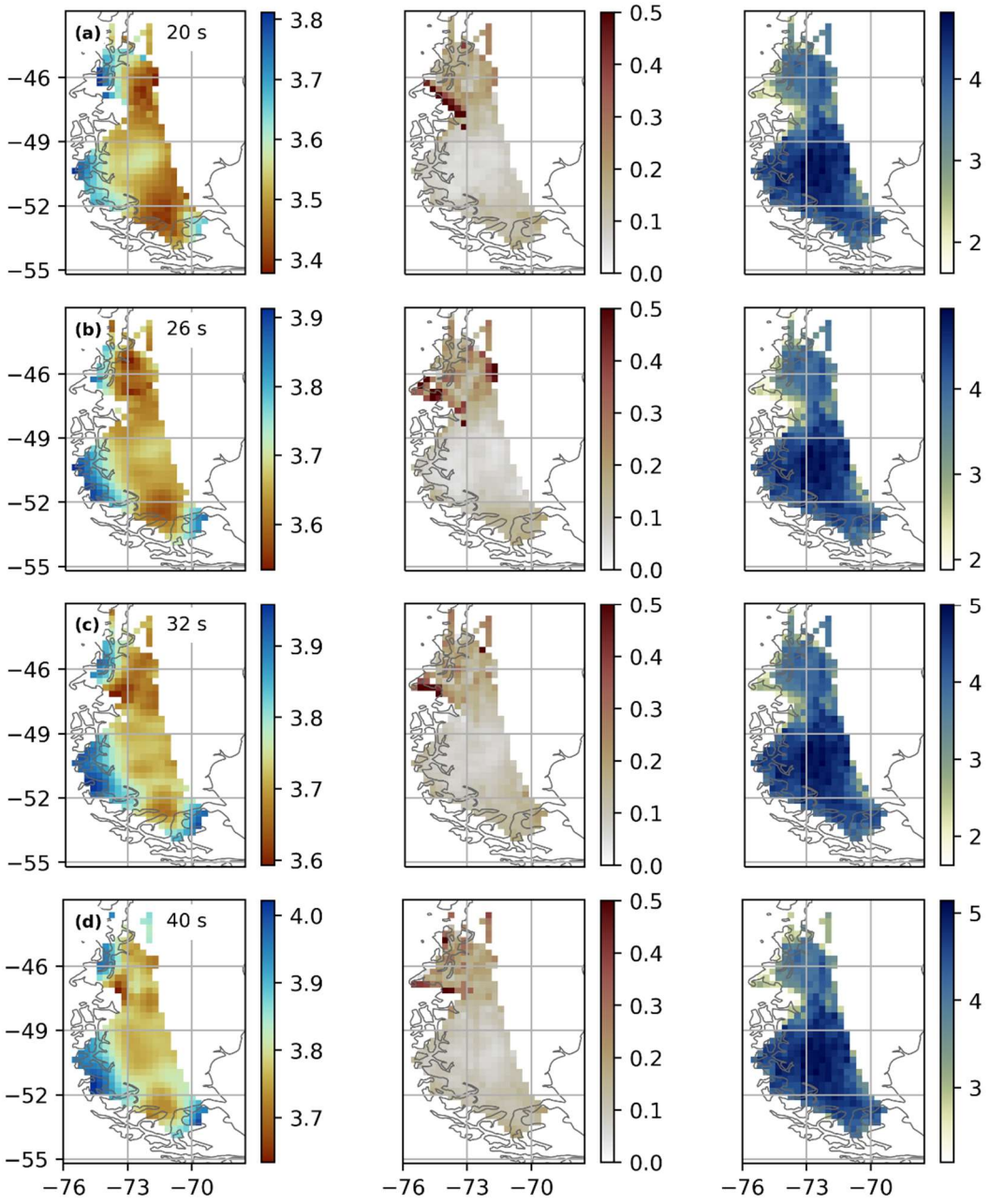

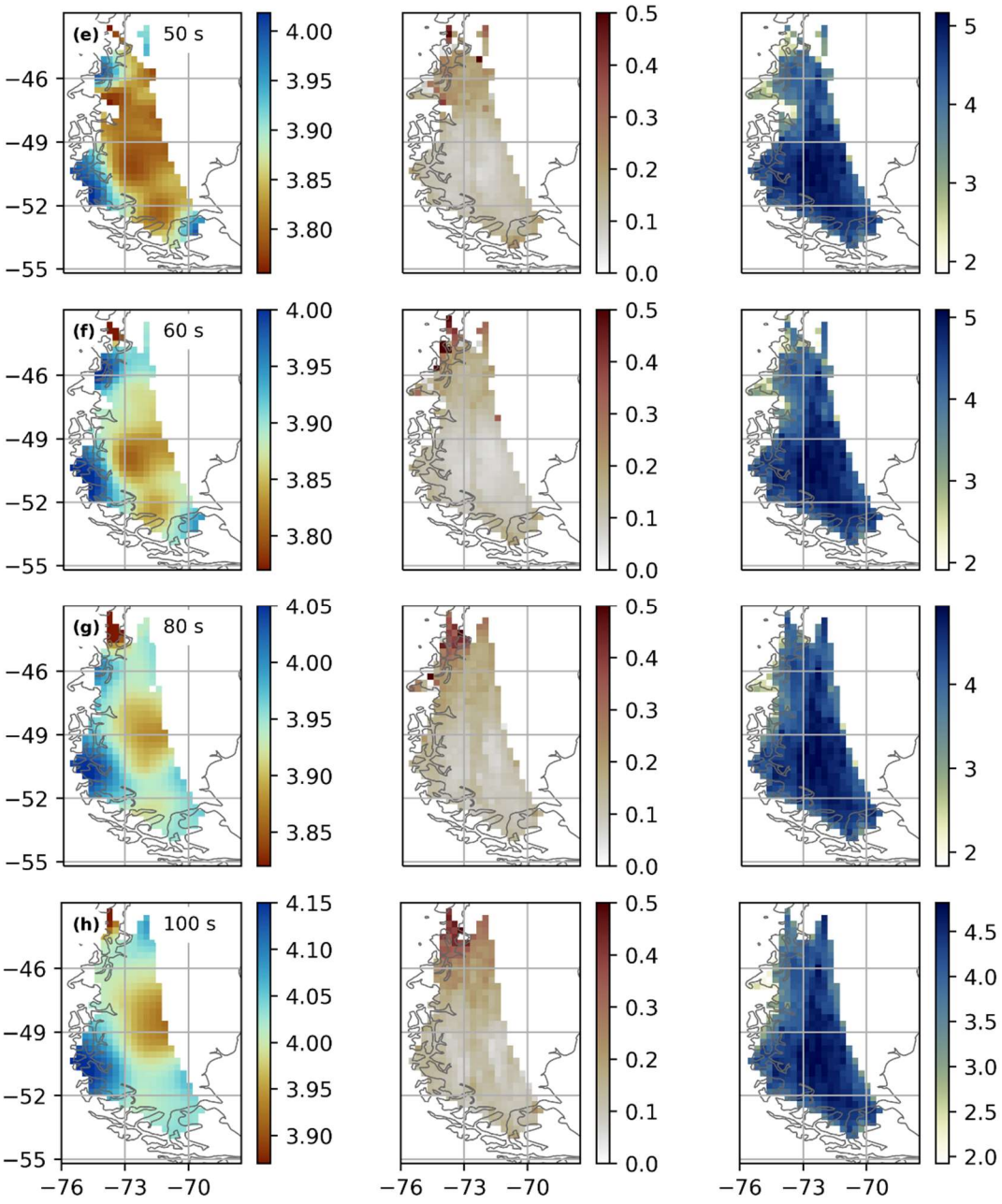

Figure S3. Phase velocity maps from earthquake tomography. The left column shows Helmholtz-corrected phase velocities in km/s, the middle column shows one standard deviation (in km/s) of the velocities calculated from stacking maps for each earthquake, and the right column shows $\log_{10}$ of the number of paths used in each grid cell. Phase velocities are shown at periods of **(a)** 20 seconds, **(b)** 26 seconds, **(c)** 32 seconds, **(d)** 40 seconds, **(e)** 50 seconds, **(f)** 60 seconds, **(g)** 80 seconds, and **(h)** 100 seconds. Velocities are only shown for grid cells where velocity measurements were obtained for at least 10 events.

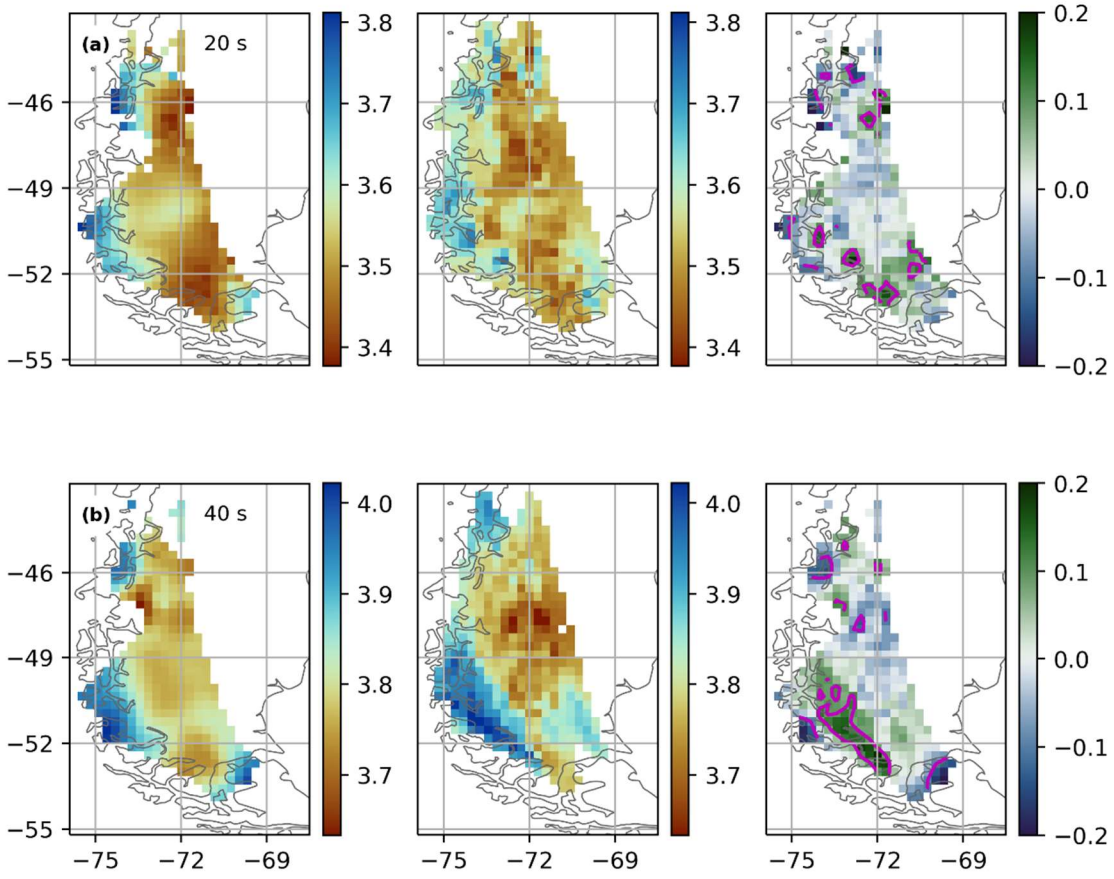

Figure S4. Comparison between earthquake and ambient noise tomography. The left column shows earthquake phase velocities as in Figure S3, the middle column shows ambient noise phase velocities as in Figure S1, and the right column shows the difference between the two velocity maps at **(a)** 20 seconds, and **(b)** 40 seconds. All velocities and velocity differences are in km/s. For the maps of velocity differences, magenta contours outline regions where the difference between the two velocity maps is greater than 0.1 km/s.

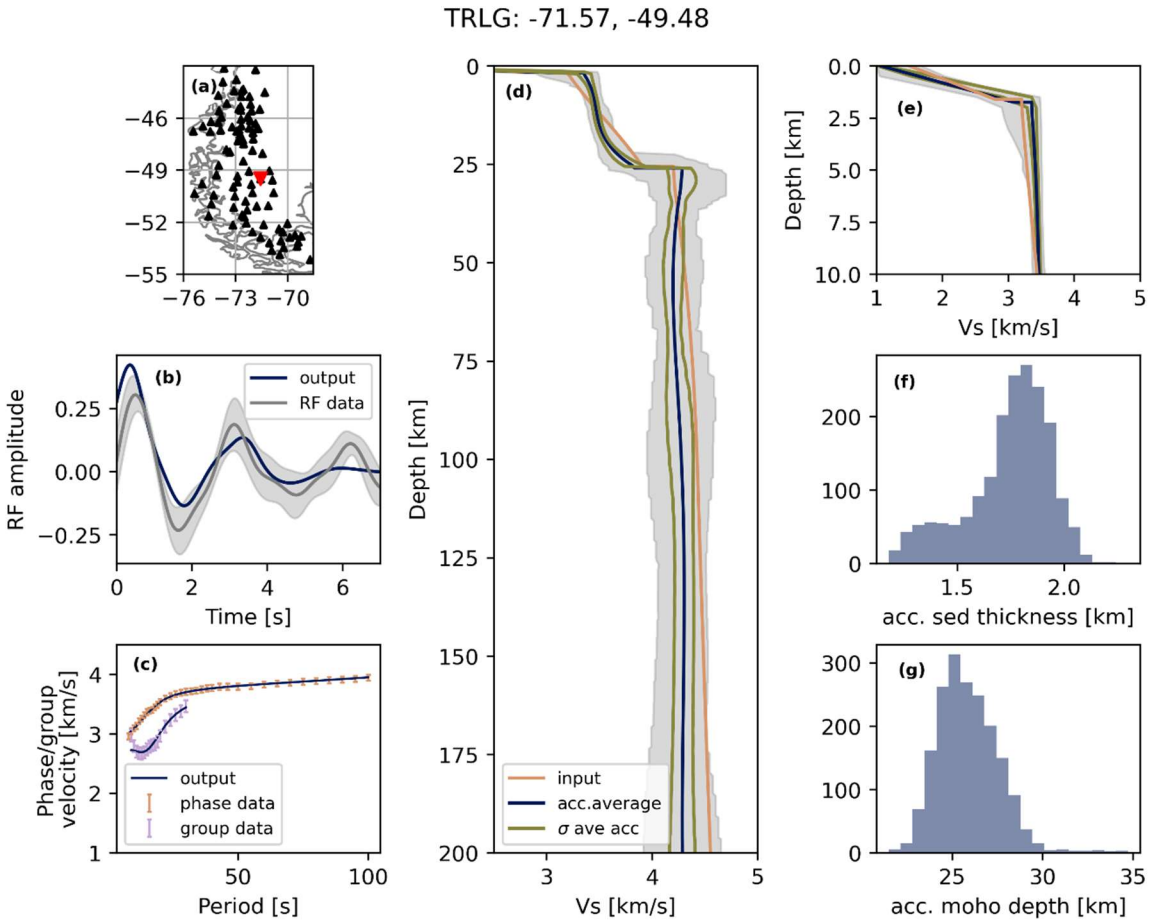

Figure S5. Inversion results for station TRLG. (a) Map showing station locations (black triangles) and the location of station TRLG (red inverted triangle). **(b)** Input station receiver function (grey line and shading) plotted with the forward-calculated receiver function for the average of all accepted velocity models for this station (dark blue line). **(c)** Input group and phase velocity measurements (pink and orange errorbars) with forward-calculated dispersion curves for the average of all accepted velocity models for this station (navy lines). **(d)** Inversion results to 200 km depth, showing the model for the centroid of the parameter prior distributions (orange line), the average of all accepted models (dark blue line), one standard deviation of all accepted models (green lines), and the range spanned by all accepted models (grey shading). **(e)** Shallow structure of accepted velocity models, with the same lines as in (d). **(f)** Histogram showing the distribution of sediment thicknesses for all accepted models. **(g)** Histogram showing the distribution of Moho depths for all accepted models.

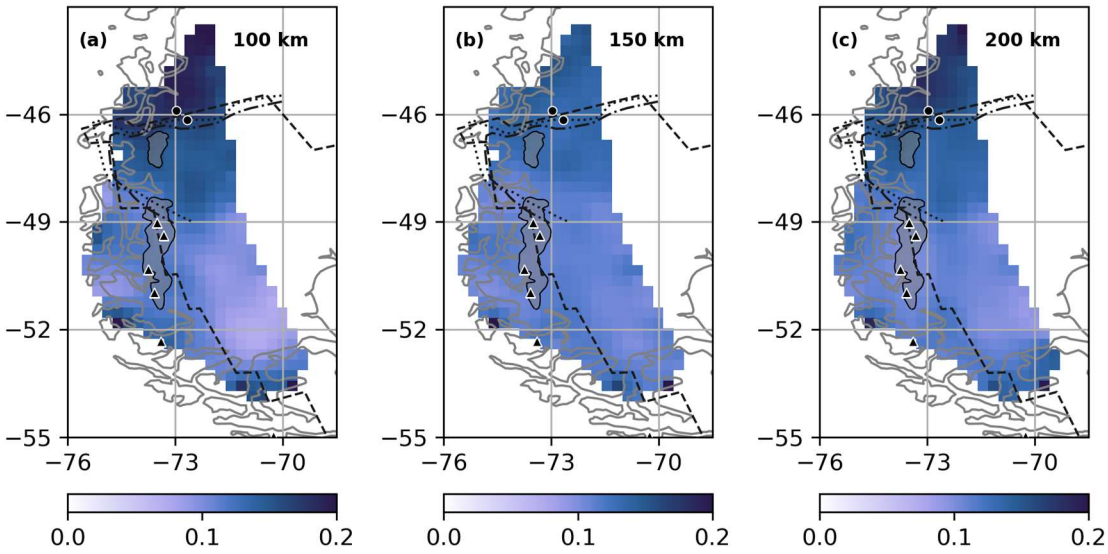

Figure S6. Velocity uncertainty maps. Maps show one standard deviation for Vsv (in km/s) at **(a)** 50 km, **(b)** 100 km, and **(c)** 150 km depth. The uncertainty maps correspond to the velocity depth slices shown in Figure 2 of the main text. On all maps, previously estimated slab window extents are shown from Russo et al. (2010) at depths of 50 km (dot-dashed line) and 100 km (dotted line), and from Breitsprecher and Thorkelson (2009) (dashed line)[1,17]. The present-day NPI and SPI are shaded in grey, and the locations of volcanoes are marked with black triangles (adakitic) and black circles (basaltic).

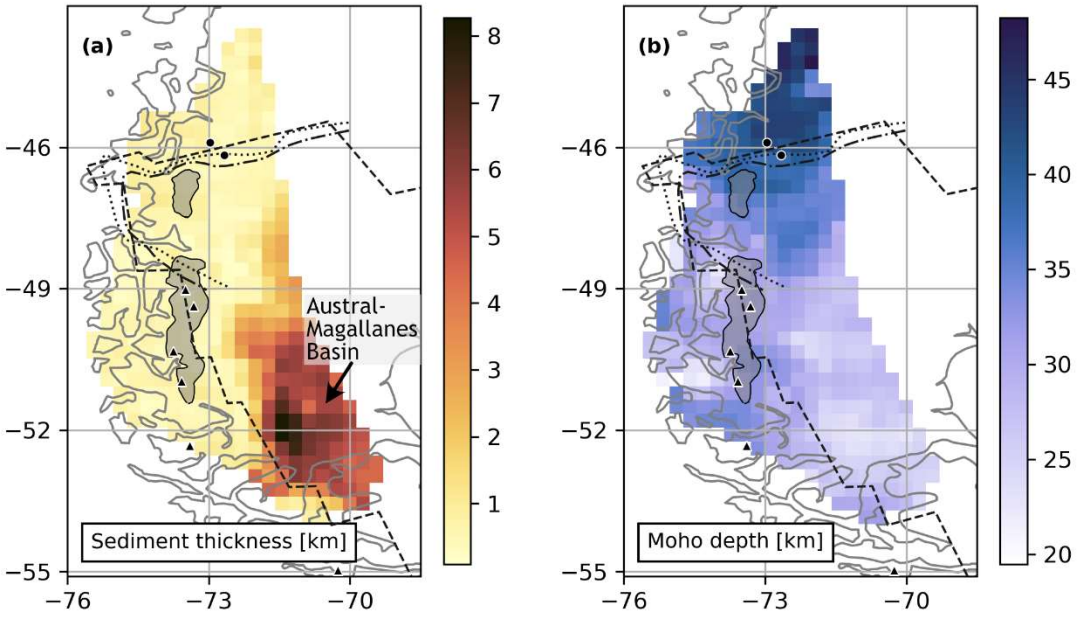

Figure S7. Sediment thickness and Moho depth from the velocity model. Maps of **(a)** sediment layer thickness and **(b)** Moho depth (sediments plus crust) show thick sediments in the Austral-Magallanes basin to the south, and a north-to-south decrease in crustal thickness across the study region. Features marked on the maps, including slab window outlines from previous studies, locations of volcanoes, and present-day icefield extents, are the same as in Figure 1. Uncertainty maps for interface depths are shown in Figure S8.

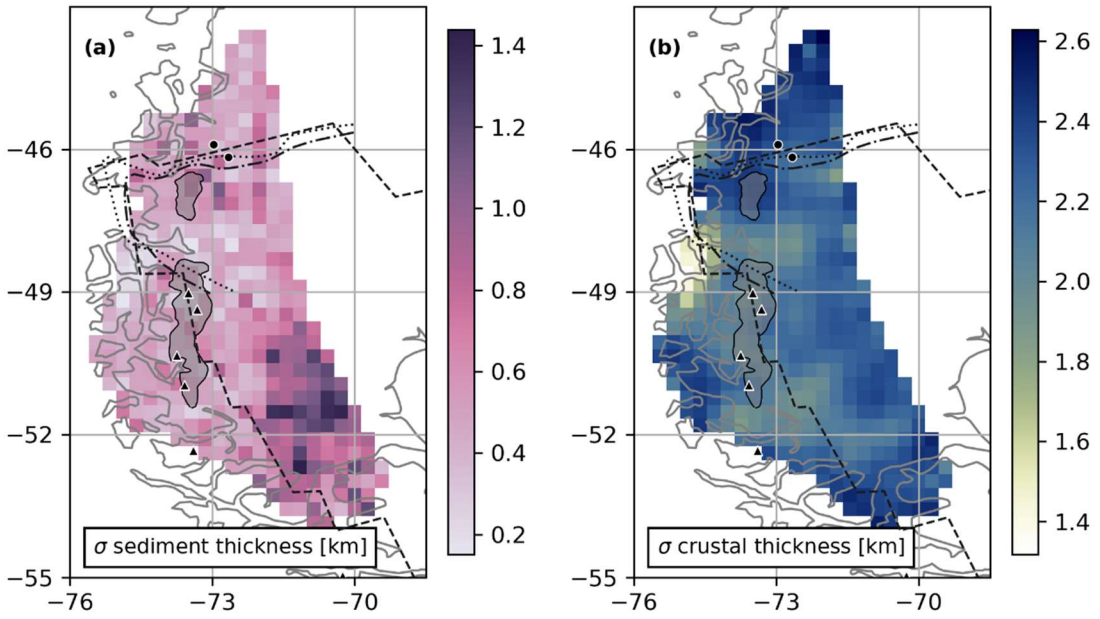

Figure S8. Sediment thickness and crustal thickness uncertainty maps. Maps show one standard deviation of **(a)** the sediment layer thickness, and **(b)** the crustal thickness, excluding sediments. Features marked on the maps, including slab window outlines from previous studies, locations of volcanoes, and present-day icefield extents, are the same as in Figure 1.

	Layer type	**Parameter**	**Value**	**Perturbation range**
Sediments	Gradient	Thickness (T_{seds})	1 or 4 km	± 1 or 4 km
		Top velocity	1.5 km/s	± 0.5 km/s
		Bottom velocity	2.2 or 2.8 km/s	± 0.6 km/s
Crust	Cubic splines	Thickness (T_{crust})	From H-k stacks	± 9 km
		1^{st} spline coeff.	3.2 km/s	± 25%
		2^{nd} spline coeff.	3.4 km/s	± 25%
		3^{rd} spline coeff.	3.6 km/s	± 25%
		4^{th} spline coeff.	3.9 km/s	± 25%
Mantle	Cubic splines	Thickness	300 km - T_{crust} - T_{seds}	
		1^{st} spline coeff.	4.2 km/s	± 25%
		2^{nd} spline coeff.	4.3 km/s	± 25%
		3^{rd} spline coeff.	4.4 km/s	± 25%
		4^{th} spline coeff.	4.5 km/s	± 25%
		5^{th} spline coeff.	4.6 km/s	± 25%
		6^{th} spline coeff.	4.7 km/s	Held constant

Table S1. Prior parameter distributions for Bayesian inversion.